RESEARCH ARTICLE

Key Points:
- CO_2 has a dominant contribution to enhanced dryland warming over East Asia, followed by black carbon (BC)
- Daily maximum and minimum temperatures show asymmetrical responses to CO_2 and anthropogenic aerosols
- CO_2 causes the diurnal temperature range (DTR) to decrease in drylands and to increase in humid regions

Correspondence to:
X. Guan,
guanxd@lzu.edu.cn

Contributions of radiative factors to enhanced dryland warming over East Asia

Yanting Zhang[1] (ID), Xiaodan Guan[1] (ID), Haipeng Yu[1], Yongkun Xie[1], and Hongchun Jin[1]

[1]Key Laboratory for Semi-Arid Climate Change of the Ministry of Education, College of Atmospheric Sciences, Lanzhou University, Lanzhou, China

Abstract Enhanced near-surface atmospheric warming has occurred over East Asia in recent decades, especially in drylands. Although local factors have been confirmed to provide considerable contributions to this warming, such factors have not been sufficiently analyzed. In this study, we extracted the radiatively forced temperature (RFT) associated with the built-up greenhouse gases, aerosol emission, and various other radiative forcing over East Asia and found a close relationship between RFT and CO_2. In addition, using climate model experiments, we explored the responses of temperature changes to black carbon (BC), CO_2, and SO_4 and found that the enhanced dryland warming induced by CO_2 had the largest magnitude and was strengthened by the warming effect of BC. Moreover, the sensitivity of daily maximum and minimum temperature changes to BC, CO_2, and SO_4 was examined. It showed asymmetric responses of daily maximum and minimum temperature to radiative factors, which led to an obvious change of diurnal temperature range (DTR), especially in drylands. The DTR's response to CO_2 is the most significant. Therefore, CO_2 not only plays a dominant role in enhanced warming but also greatly affects the decrease of DTR in drylands. However, the mechanisms of these radiative factors' effects in the process of DTR change are not clear and require more investigation.

1. Introduction

Asia is arguably the most sensitive area to climate change because it accounts for almost 39% of the world's land area [*White and Nackoney*, 2003; *Huang et al.*, 2013], contains large arid and semiarid regions [*Huang et al.*, 2014], and supports 67% of the world's population [*Guan et al.*, 2015]. A large portion of the drylands in Asia exhibits significantly enhanced near-surface warming in the boreal cold season [*Huang et al.*, 2012], which will make the areas more arid [*Wang et al.*, 2012] and accelerate the expansion of drylands [*Huang et al.*, 2016]. In fact, enhanced dryland warming has been reported at global scale [*Huang et al.*, 2012; *Zhou*, 2016], and the warming rate changes with altitude [*Santer et al.*, 2005; *Cook and Vizy*, 2015]. The warming rate of near-surface air temperature depends on surface radiative forcing [*Hansen et al.*, 2010; *Thorne et al.*, 2010; *Wang and Dickinson*, 2013]. To understand the warming mechanism over drylands, many researchers examined the changes of surface energy budget [*Cook and Vizy*, 2015; *Zhou*, 2016; *Zhou et al.*, 2016]. *Zhou et al.* [2016] found that greenhouse gases (GHGs) enhanced downward longwave radiation (DLR) are the primary driver for desert amplification through a comprehensive analysis. DLR displays a persistent increasing trend, while downward shortwave radiation varies slightly and has a secondary effect [*Zhou*, 2016].

Enhanced dryland warming may be affected by various dominant factors, including circulation dynamical adjustment, sea surface temperature anomalies, land and atmosphere interactions, snow and frozen soil cover changes, and regional human activities [*Hu and Gao*, 1994; *Zhang et al.*, 2001; *Huang et al.*, 2008; *Guan et al.*, 2009; *He et al.*, 2014]. Especially in the cold season, snow-albedo feedback may play an important role. As the enhanced warming in winter may cause a decline of snow/ice and frozen ground, it would decrease surface albedo, absorbing more solar energy and causing the temperature to increase. *Guan et al.* [2015] found that the enhanced warming in the drylands was a result of radiatively forced temperature, which has a close relationship with human activities and aerosol column burden. Moreover, the rapid economic development in Asia has led to increased consumption of fossil fuel, which has generated a considerable amount of GHGs and energy [*Barnett and O'Neill*, 2010], and the spatial distribution of temperature has been greatly influenced by the GHGs released in recent years [*Li and Zhao*, 2012].

GHGs and aerosols are the two most important forcing agents associated with human activities [*Myhre et al.*, 2013; *Lin et al.*, 2016a], and they have strong influences on temperature changes. The Intergovernmental

Panel on Climate Change (IPCC) Fifth Assessment Report (AR5) [*Stocker et al.*, 2013] notes that the radiative forcing of well-mixed GHGs has greatly increased and can reach 3 W m^{-2}. Among all the radiative forcing factors, increased CO_2 has the largest contribution. Its radiative forcing is 1.68 W m^{-2}, which can reach 1.82 W m^{-2} when considering other carbon-containing gases that can increase the CO_2 concentration [*Stocker et al.*, 2013]. Model simulation results also show that increases in CO_2 will induce a mean terrestrial aridity decrease; thus, land areas will become drier [*Feng and Fu*, 2013; *Lin et al.*, 2016b]. Because of the impacts of GHGs on global precipitation patterns as well as fertilization effect, increases in GHGs, such as CO_2, may further influence the vegetation of drylands [*Ukkola et al.*, 2015; *Lu et al.*, 2016].

In addition, aerosols play a substantial role in climate change, especially regarding the obvious warming effect in drylands [*Huang et al.*, 2006, 2008; *Chen et al.*, 2010; *Ye et al.*, 2012; *Jin et al.*, 2015]. They tend to have a relatively large optical depth [*Huang et al.*, 2010; *Bi et al.*, 2011; *Liu et al.*, 2011; *Xu and Wang*, 2015; *Xu et al.*, 2015], which leads to a significant radiative effect on drylands. Generally, the aerosols in drylands are divided into two categories: natural and anthropogenic aerosols. Asia is a heavy aerosol-laden region with increasing trends of both desert dust and anthropogenic emission [*Hsu et al.*, 2012], and anthropogenic aerosols may play a major role according to *Guan et al.* [2016]. With intense human activity and rapid economic development, anthropogenic aerosol emissions have likely increased over different regions [*Mahowald and Luo*, 2003], and such increases can promote aerosol loading and affect radiative forcing [*Huang et al.*, 2015a].

Black carbon (BC) aerosols are significant contributors to anthropogenic climate changes; they are considered as the second largest warming agent following CO_2 [*Xu*, 2014], with a global mean climate forcing of 1.1 W m^{-2} [*Bond et al.*, 2013]. More than 50% of the global anthropogenic BC emission is from China and India [*Xu*, 2014]. Thus, on a regional scale, particularly for the regions in Asia, BC aerosols have a large impact on the climate system, including the Earth's radiative balance, monsoon variability [*Lau et al.*, 2010], and tropical cyclone activity [*Evan et al.*, 2011]. BC can absorb incoming solar radiation, and warm the air; and the deposition of BC on snow/ice significantly darkens the surface, thereby altering surface albedo and accelerating the melting of snow. The melting snow in response to the above mentioned heating mechanisms will further decrease surface albedo, which then forms a positive feedback [*Xu et al.*, 2016]. So the largest response of surface temperature to BC appears in snow/ice. There are many field campaigns and model simulations, which have been conducted to measure the impact of BC on snow [*Ye et al.*, 2012; *Wang et al.*, 2013; *Zhao et al.*, 2014; *Xu et al.*, 2016].

Another major anthropogenic aerosol is sulfate (SO_4), which is mainly generated via industrial sulfur dioxide (SO_2) emission [*Qian and Fu*, 1997]. SO_4 aerosols can reduce the shortwave radiation reaching the surface via scattering and reduce global precipitation [*Lin et al.*, 2016c]. They are also effective cloud condensation nuclei and ice nuclei for homogeneous freezing; therefore, they have a large impact on cloud droplet size, known as an indirect aerosol effect [*Twomey*, 1977], which further brightens clouds and cools the climate by reflecting more solar radiation back to space. SO_4 and BC are two important aerosol species over East Asia, and they represent nonabsorbing and absorbing aerosols, respectively [*Gao et al.*, 2014].

East Asia is simultaneously experiencing rapid economic growth and enhanced warming. More anthropogenic GHGs and aerosols are released into the atmosphere as the consequences of social-economy development, but the separate impacts of these radiative factors on temperature changes remain poorly understood. In this study, the contributions of CO_2, BC, and SO_4 aerosols to enhanced dryland warming are explored by using historical emission data and a Community Earth System Model (CESM) sensitivity test. In section 2, we introduce the data sets and methods used in this study. In section 3, we present the observed enhanced dryland warming in East Asia. In section 4, we analyze the responses of surface air temperature to CO_2, BC, and SO_4, and their combined effects. Conclusions and discussion are presented in section 5.

2. Data and Methods

2.1. Aridity Index Data Set

In this study, the aridity index (AI) is used to classify climate types of different regions. The AI is defined as the ratio of annual precipitation to annual potential evapotranspiration. It represents the degree of climatic dryness; hence, a smaller AI indicates a drier region. The AI data set [*Feng and Fu*, 2013] used in this study is based on the Climate Prediction Center data set. Drylands are identified as regions with AI < 0.65, and

they are further classified into hyperarid (AI < 0.05), arid ($0.05 \leq$ AI < 0.2), semiarid ($0.2 \leq$ AI < 0.5), and dry subhumid ($0.5 \leq$ AI < 0.65), following the classification of *Middleton and Thomas* [1997]. The AI data set covers the period from 1948 to 2008 and has a spatial resolution of 0.5° by 0.5°.

2.2. Temperature Data Set

The observed temperature used in this study is the monthly mean surface air temperature of the land-only TS3.21 data set obtained from the Climate Research Unit at the University of East Anglia [*Mitchell and Jones*, 2005]. The dynamical adjustment method [*Wallace et al.*, 2012] is used to divide the raw temperature into two parts: dynamically induced temperature (DIT) and radiatively forced temperature (RFT). The separate DIT and RFT data sets are provided by *Guan et al.* [2015], and they cover the period from 1902 to 2011 with a spatial resolution of 0.5° by 0.5°.

2.3. CMIP5 Historical Emission Data

BC and SO_2 emissions are from the standard inventory adopted by the Climate Model Intercomparison Program #5 (CMIP5) in support of the IPCC AR5 as described in *Lamarque et al.* [2010]. Both BC and SO_2 emissions are mainly anthropogenic emissions. The inventory covers the period from 1850 to 2000 in terms of monthly mean, which changes once every 10 years, and the spatial resolution is 0.5° by 0.5°. In addition, the annual CO_2 concentration is used to calculate its correlation with RFT. The CO_2 concentration for the period of 1950–2005 is from the CMIP5 historical simulation data set, and that for the period of 2006–2011 is from the Representative Concentration Pathway (RCP) 8.5 simulation data set.

2.4. Global Climate Model Experiment

We used the simulation results of the CESM1 provided by *Xu and Xie* [2015], with a finite-volume nominal 1° horizontal resolution (0.9° by 1.25°). The CESM1 is a coupled ocean-atmosphere-land-sea ice model that includes the forcing of GHGs [*Lamarque et al.*, 2010]. CESM1 climate simulations have been documented extensively [*Meehl et al.*, 2013]. In CESM1, the overall climate system response including forcing and feedback is much improved compared to the previous model version [*Meehl et al.*, 2013]. A new cloud microphysics scheme [*Morrison and Gettelman*, 2008] was applied in the model. Aerosol concentrations can affect the number concentration of cloud droplets and ice crystals; thus, the "indirect radiative forcing" of aerosols is included in the model. It was also validated by comparing the climatology of temperature [*Xu et al.*, 2016] and aridity [*Lin et al.*, 2015] against observations. The model simulation data set used in this paper has been used in many other studies, such as aridity analysis [*Lin et al.*, 2016c], high-altitude warming [*Xu et al.*, 2016], and ocean mediation of tropospheric response [*Xu and Xie*, 2015] to radiative factors.

In this study, mainly two sets of model experiments are used: a control simulation for the preindustrial climate and four sets of perturbed simulations (BC, SO_4, CO_2, and all three forcings combined). The control simulation is a 319 yearlong preindustrial control run, which was extended with an additional 75 year run to test whether a discernible drift occurred in the mean climate state. In the four sets of the perturbed simulations, the forcing was imposed by instantaneously increasing the emission of BC, the emission of the precursor to SO_4 (SO_2), or the concentration of CO_2 to the present-day level (400 ppm), and then running the perturbed simulations in the fully coupled mode for 75 years, which started from the end of the 319th year of the control simulation. Except for the adjusted BC present-day emission from the standard emission inventory to account for the potential underestimation of BC emissions [*Xu et al.*, 2013], all other emissions are from the standard inventory adopted by the CMIP5 models [*Lamarque et al.*, 2010]. To increase the signal-to-noise ratio in the BC case (due to a smaller BC forcing), five ensembles of perturbed simulations were conducted. Long averaging time enables us to dampen the influence of decadal natural variability, such as that in the atmospheric circulation, and to obtain a clear effect due to aerosol perturbation. So we calculate the difference between the last 60 years (the first 15 years are considered as the model spin-up period) of the perturbed simulations and the long-term control simulation to provide the respective response signal caused by the imposed forcing [*Xu et al.*, 2016].

2.5. Methods

Guan et al. [2015] successfully divided the raw temperature into DIT and RFT using the dynamical adjustment method. This method was first proposed by *Wallace et al.* [2012] to analyze the nonuniformity of spatial
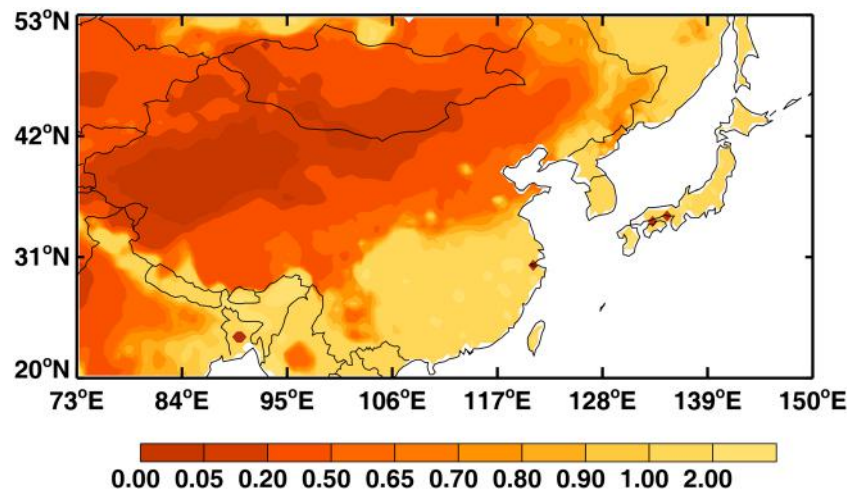
Figure 1. Spatial distribution of annual-mean AI from 1948 to 2008 over East Asia.

warming over the Northern Hemisphere, and it was subsequently improved by *Smoliak et al.* [2015]. The sea level pressure (SLP) data and high-pass-filtered surface air temperature time series were first standardized, and then the surface air temperature was regressed to the SLP using a partial least squares approach in a pointwise manner. After that, the DIT variability associated with changes of atmospheric circulation patterns was partitioned, and the residual part was the RFT. The RFT is associated with GHGs, volcanic eruptions, aerosol emissions, and local anthropogenic forcing.The study area is 73–150°E and 20–53°N, as shown in Figure 1. The regionally average temperature of region k is calculated as follows:

$$\overline{T}_k = \frac{\sum_{i=1}^{N_k} W_{ki} \times T_{ki}}{\sum_{i=1}^{N_k} W_{ki}} \tag{1}$$

where N_k is the number of grids in region k, T_{ki} is the temperature at grid i in region k, and $W_{ki} = \cos(\theta_i \times \pi/180)$, where θ_i is the latitude of grid i.

3. Observed Enhanced Dryland Warming

The distribution of the 61 year averaged AI in East Asia from 1948 to 2008 is shown in Figure 1. It illustrates that most of the drylands are located in the northwest and the humid regions are located in the southeast. The arid and semiarid regions account for the greatest area of East Asia, and AI shows a general increasing pattern from northwest to southeast. According to *Huang et al.* [2012], the warming trend in Asia was particularly enhanced in the boreal cold season over semiarid regions. Using the dynamical adjustment method [*Wallace et al.*, 2012], *Guan et al.* [2015] successfully demonstrated that RFT plays a dominant role in the enhanced warming in East Asia. However, they only analyzed data via statistical approach and did not qualify the warming effects of individual radiative factors.

Huang et al. [2015b] reported that the climate over East Asia became drier in the recent 60 years, dominated by a weakened East Asian summer monsoon. To ensure the quality of the data set [*Mitchell and Jones*, 2005; *Zhou*, 2016], we choose the data set from 1950 to 2011 in our study. Figure 2 shows the spatial distribution of the raw temperature, the DIT and RFT trends over East Asia in winter between 1950 and 2011. Figure 2a illustrates the gradually increasing warming pattern from south to north with the strongest warming trend over northern East Asia, especially in the Junggar Basin and Northeast China. The distribution of the RFT trend (Figure 2c) exhibits a similar distribution to that of the raw temperature, and obvious warming occurred over the northern area of East Asia, which reached 0.05°C yr^{-1} in some regions. The distribution of the DIT trend (Figure 2b) is quite different from that of the raw temperature and likely presents a basic warming background over East Asia.
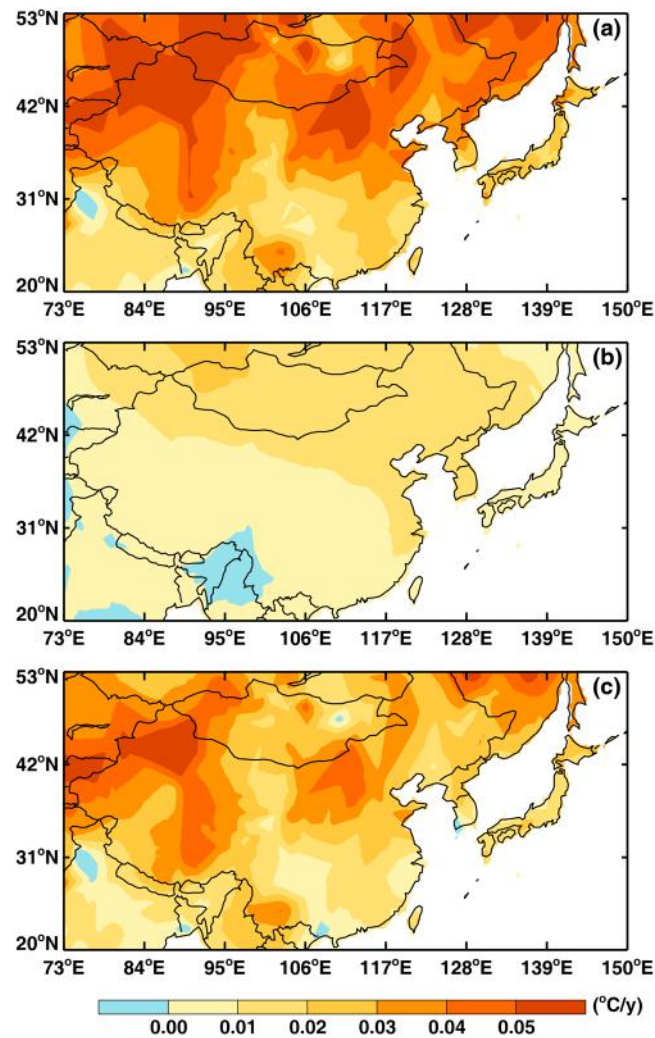
Figure 2. Spatial distributions of (a) raw, (b) dynamically induced, and (c) radiatively forced temperature trends (°C/yr) in winter from 1950 to 2011 over East Asia.
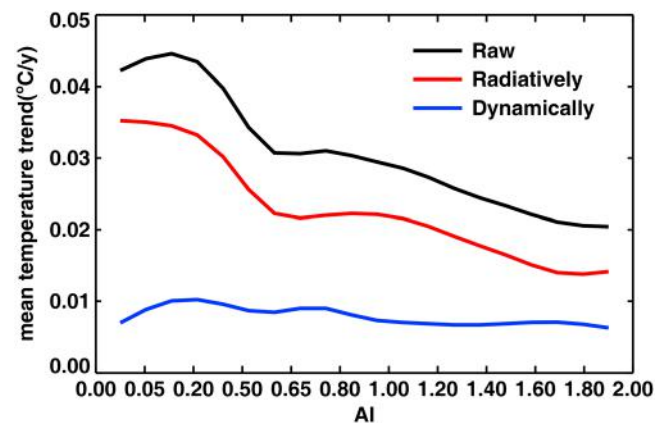

Figure 3. Regionally averaged temperature trend as a function of annual-mean AI for raw (black), dynamically induced (blue), and radiatively forced (red) temperatures in winter from 1950 to 2011 over East Asia.

Figure 3 shows the long-term trends of raw temperature, RFT, and DIT in winter as a function of annual-mean AI. Both the raw temperature and RFT reaches peak in the area with the AI between 0 and 0.2. The trend of the DIT does not show a distinct difference over different climate regions, which indicates that the RFT accounts for a major contribution to the regional temperature variation. Compared with the results presented in Figure 2, the trend in Figure 3 suggests that radiative factors have a dominant role in the enhanced warming observed over the drylands. Variability in RFT is usually closely associated with GHGs, aerosols [*Huang et al.*, 2011; *Li et al.*, 2011; *Guan et al.*, 2016], land use cover changes, decreased albedo, clouds [*Huang et al.*, 2005, 2006], and regional human activity. With the rapid economic development and industrialization of East Asia, a large number of anthropogenic GHGs, especially CO_2 and aerosols, are being produced and released into the atmosphere, and eventually impact local climate [*Qian et al.*, 2009, 2011]. Therefore, it is necessary to qualify the response of surface temperature to these radiative factors. In this study, three representative factors of CO_2, BC, and SO_4 are chosen to explore the response of surface air temperature.

4. Contributions of Radiative Factors to Enhanced Dryland Warming

4.1. Individual Roles of Radiative Factors

Figure 4a shows the distribution of the correlation coefficient between detrended CO_2 and detrended RFT, with the stippling indicating the 95% confidence level. As CO_2 is a typical GHG with a broad influence on warming, we chose the time series of CO_2 and calculated its relationship with RFT. The correlation coefficients present confidence levels that are higher than 95% in most regions of East Asia, and they are primarily centered in central China and western China, with the largest
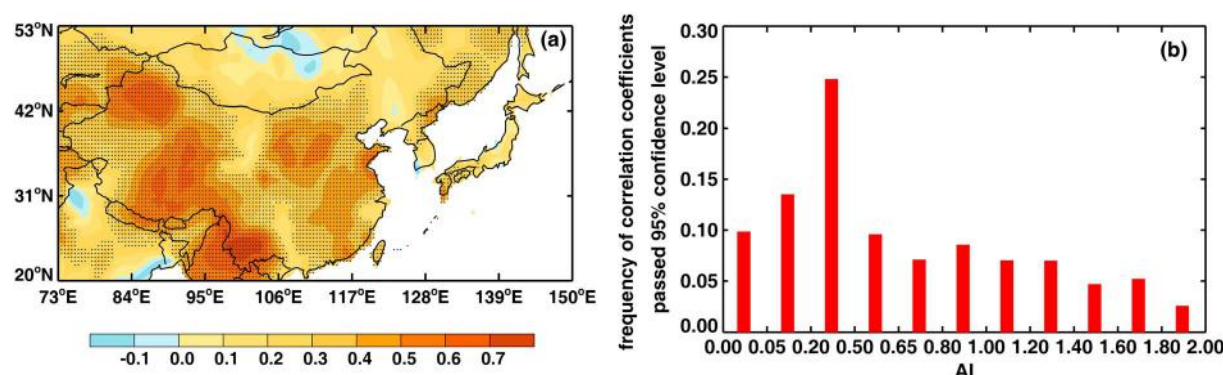
Figure 4. (a) Spatial distribution of correlation coefficient between detrended CO_2 and detrended radiatively forced temperature in winter from 1950 to 2011 over East Asia. Grid points in Figure 4a are stippled for statistically significant changes based on the 95% confidence interval from a two-sided t test. (b) Frequency of correlation coefficients passed the 95% confidence level as a function of the annual-mean AI.

correlation coefficient reaching 0.77. Figure 4b shows the correlation coefficients passing the 95% confidence level as a function of AI. They mainly concentrated on semiarid regions. More than half of the correlation coefficients in drylands pass the 95% confidence level. It suggests that the enhanced dryland warming may have a close relationship with CO_2.

Besides CO_2, BC is a popular warming aerosol. Figure 5a is the regionally averaged BC emission as a function of the AI. It shows that most high concentration of BC is distributed in humid regions; the value is much higher than that in arid and semiarid regions. Most of the BC emissions in drylands (with AI < 0.5) is less than 1×10^{-5} kg m^{-2}. The largest regionally averaged BC emission observed in humid regions is located in region where the AI is between 1.4 and 1.6, with the value of BC reaching 7.6×10^{-5} kg m^{-2}, which is almost 10 times larger than the regionally averaged BC emissions in arid and semiarid regions. This discrepancy is related to production of the BC emission by China. BC emissions are mainly from the industrial and residential sectors [*Xu*, 2014], and eastern China is a relatively developed area than the western arid regions in terms of industry and population. The distribution of mean temperature's response to BC changes as a function of BC emission (Figure 5b) emphasizes BC's influence on temperature of drylands. The regions with low BC emission (less than 1×10^{-5} kg m^{-2}) have greater temperature responses compared the regions with high BC emission. The areas with BC emission less than 1×10^{-5} kg m^{-2} are mainly distributed in arid and semiarid regions. It suggests that the temperature in arid and semiarid regions is more sensitive to BC emission than that in humid regions.

SO_4 is another important aerosol species over East Asian, representing nonabsorbing aerosols. Figure 6 shows the SO_2 (SO_4's precursor) concentration distribution as a function of the AI (Figure 6a) and the mean
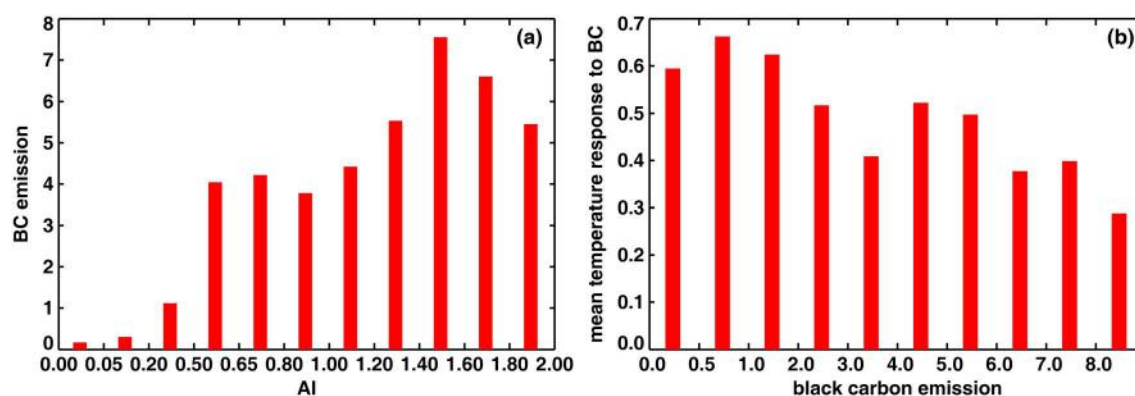

Figure 5. (a) Regionally average black carbon emission (total emissions of January, February, and December in year 2000, units: 10^{-5} kg m^{-2}) as a function of annual-mean AI over East Asia. (b) Mean temperature response (°C) to BC as a function of the BC emission over East Asia by calculating the difference of mean temperature for 60 years between perturbation simulation and the preindustrial control run.
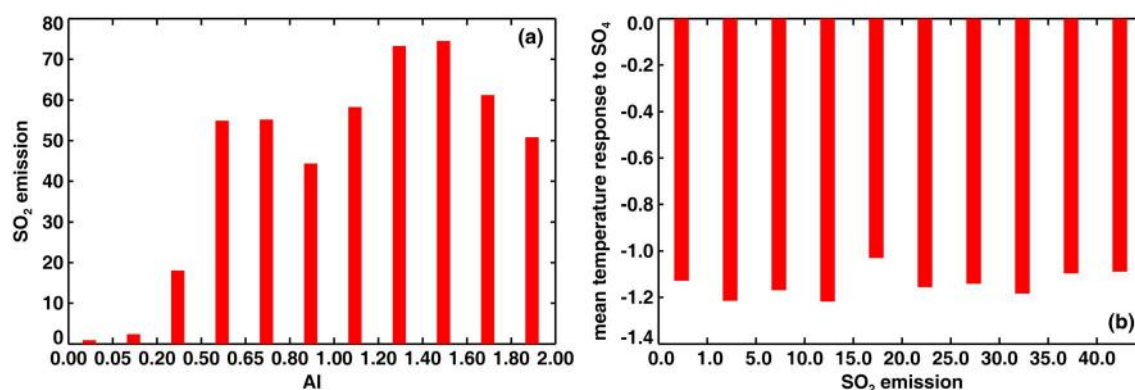
Figure 6. Same as Figure 5 except for SO_2 (units: 10^{-5} kg m^{-2}).

temperature response to SO_4 as a function of SO_2 emission (Figure 6b). The SO_2 emission is higher than the BC emission, although their distributions are similar. In arid regions with AI less than 0.5, the SO_2 emission is low, whereas in humid regions, the SO_2 emission is much higher. The humid regions are mostly located in the eastern part of East Asian, which is more developed; therefore, there are higher anthropogenic aerosol emissions in the humid regions. Significant differences are not observed in the mean temperature response to SO_4 aerosols as a function of SO_2 emission. Therefore, although the SO_4 emission over drylands is much lower than that in humid regions, the temperature response is comparable.

4.2. Mean Temperature Response

To determine the relative roles of CO_2, BC, and SO_4 in temperature changes, we calculated the temperature response to the three forcing factors individually. The temperature response is the difference of mean temperature over 60 years between perturbed simulation and the preindustrial control run. In the model simulation, the forcings were imposed by instantaneously increasing the emissions of CO_2/BC/SO_4's precursor to present-day levels. Therefore, the model output is not aiming at reproducing the reality during the twentieth century, but at understanding surface air temperature's responses to different radiative factors. Figure 7 shows distributions of the mean temperature (°C) responses in winter to CO_2 (Figure 7a), BC (Figure 7b), SO_4 (Figure 7c), and all three forcing factors combined (Figure 7d), with the 95% confidence from a two-sided t test covering most of the region.

In response to CO_2, the mean temperature shows a warming pattern over all East Asia (Figure 7a). The temperature increase is greater in the northwest arid regions, and a large center is located in Inner Mongolia and Xinjiang Uyghur Autonomous Region. Model simulation results show that the increase in CO_2 would make land areas drier [*Lin et al.*, 2016b]; thus, it may lead to an expansion of drylands. Expansion of drylands will further result in reduced carbon sequestration and enhanced regional warming [*Huang et al.*, 2012; *Ji et al.*, 2014], causing more sensitive temperature response to CO_2 over drylands than over humid regions [*Huang et al.*, 2016]. For the effect of BC on temperature, Figure 7b shows a temperature increase over almost all East Asia, with a slight decrease over India and Burma. In addition, the BC warming magnitude is relatively smaller compared to that of CO_2, and a greater center is located over Tibet and Northeast China. This is because the temperature response to BC is larger in regions with snow and ice [*Xu et al.*, 2016].

The cooling effect of SO_4 on surface air temperature (Figure 7c) is greater in Northeast and Southeast China than in the other regions because of the high concentration of sulfate aerosols in these regions. There is also a large center in the Tibet Plateau, which is similar to the result of *Kasoar et al.* [2016]. It illustrates that the temperature response is not only related to SO_4 concentration but also influenced by clouds via SO_4, atmospheric circulation, and other factors. Figure 7d shows the temperature response to the combined forcing, which has a warming effect on temperature, and an obvious decreasing pattern from the northwest to the southeast. To further explore temperature response over different climate regions, the regionally averaged mean temperature responses to CO_2, BC, and SO_4 are illustrated in Figure 8. The increased temperatures induced by BC, CO_2, and the combined forcing are greater in drylands than in humid regions, especially in arid and
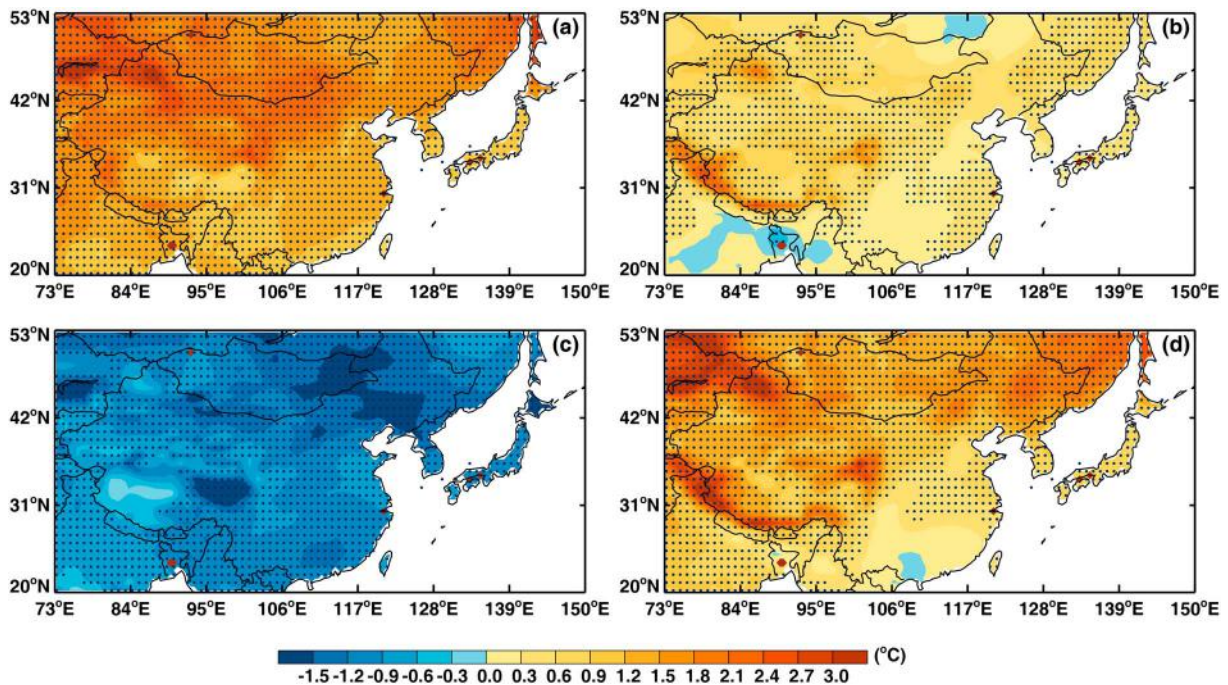
Figure 7. Distributions of mean temperature (°C) responses in winter to (a) CO_2, (b) BC, (c) SO_4, and (d) the combined forcing over East Asia. Grid points are stippled for statistically significant changes based on a 95% confidence interval from a two-sided *t* test.

semiarid regions. The warming effect of CO_2 is the largest, followed by that of BC. Comparing the responses to CO_2, BC, and SO_4, we can see that the enhanced dryland warming is mainly induced by CO_2, followed by BC. Although SO_4 has a larger effect on temperature than BC, its effect on drylands does not have an obvious difference with that on humid regions. So SO_4 does not appear to play an important role in the enhanced dryland warming.

4.3. Diurnal Temperature Range Response

As the mean temperature is related to daily maximum and minimum temperatures, the effects of the radiative factors may impact both daily maximum and minimum temperatures [*Guan et al.*, 2015]. Therefore, we show the distributions of daily maximum temperature responses in winter to CO_2 (Figure 9a), BC (Figure 9b), SO_4 (Figure 9c), and the combined forcing (Figure 9d),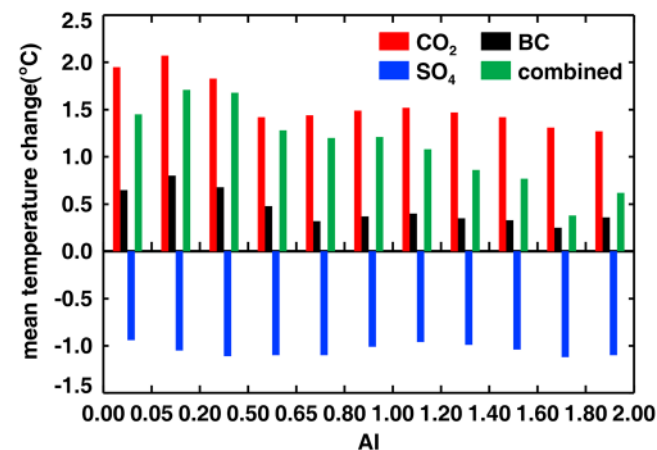 and the distributions of daily minimum temperature responses (Figure 10). In general, the distributions are all similar to those of the mean temperature (Figure 7). However, for the temperature response to CO_2, the daily maximum temperature distribution (Figure 9a) is more uniform compared with the daily minimum temperature distribution (Figure 10a). The daily minimum temperature response to CO_2 (Figure 10a) is stronger in Northwest China and smaller in Southeast China compared with the results of daily maximum temperature shown in Figure 9a. Such asymmetrical changes in daily maximum and minimum temperatures will directly induce changes in diurnal temperature range (DTR).
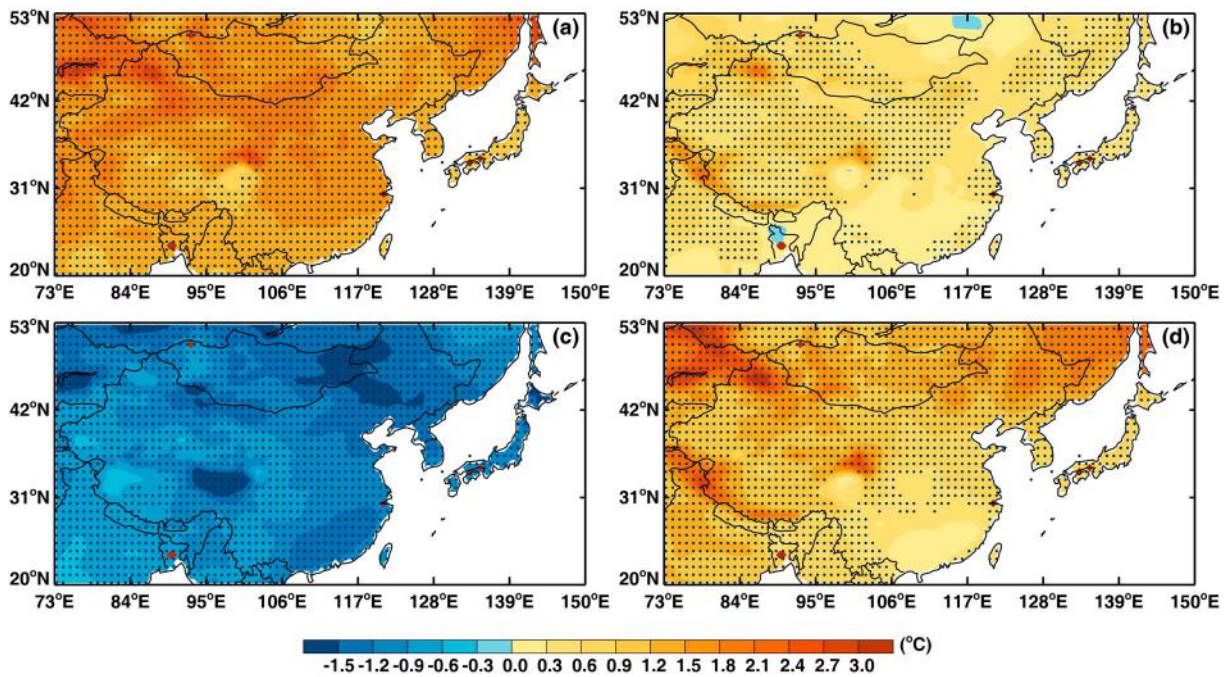

Figure 8. Regionally average mean temperature (°C) responses in winter to CO_2 (red), BC (black), SO_4 (blue), and the combined forcing (green) as a function of annual-mean AI over East Asia.

Figure 9. Same as Figure 7 except for daily maximum temperature (°C).

The distributions of DTR responses in winter to CO_2 (Figure 11a), BC (Figure 11b), SO_4 (Figure 11c), and the combined forcing (Figure 11d) are also shown. The DTR response to CO_2 (Figure 11a) is decreased in the northwest drylands and increased in the southeast humid regions, with the boundary along the Taihang Mountains. Most of the areas pass the 95% confidence level. The DTR response to BC (Figure 11b) is decreased in most regions, although an increase is observed in central and West China and in most regions of Inner Mongolia, with a small area of the DTR's response to BC passing the 95% confidence level. The DTR response to SO_4 (Figure 11c) is nearly opposite to the response to CO_2, with an increase in the arid region of
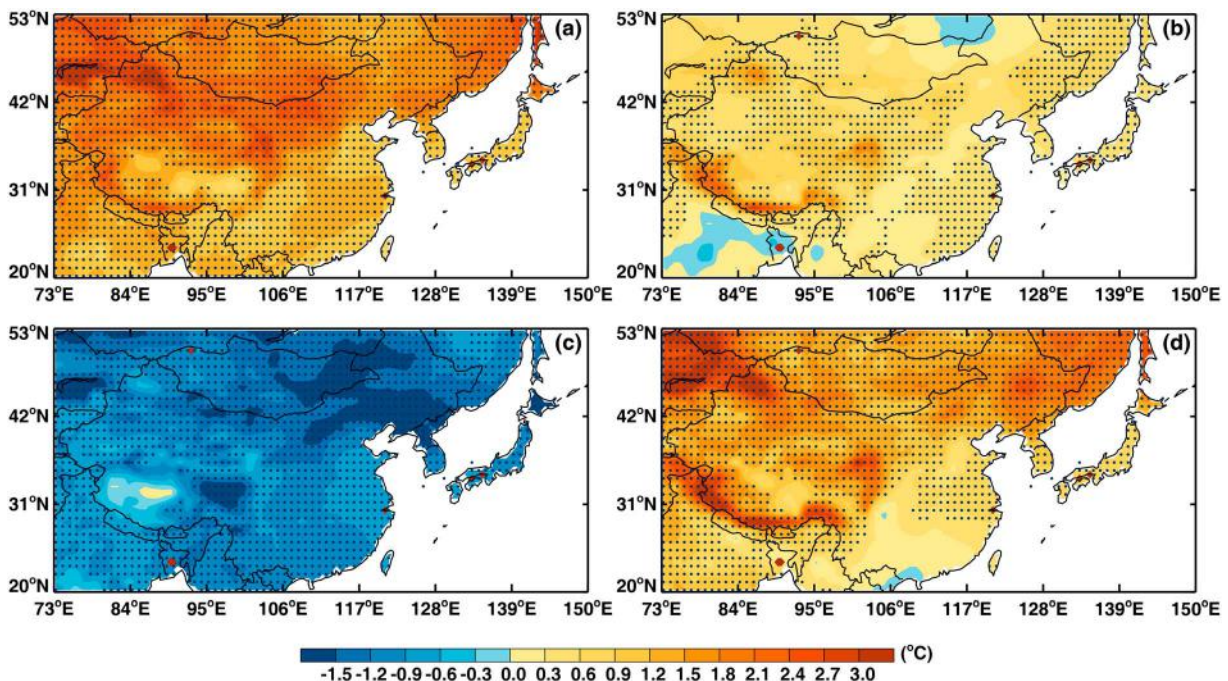

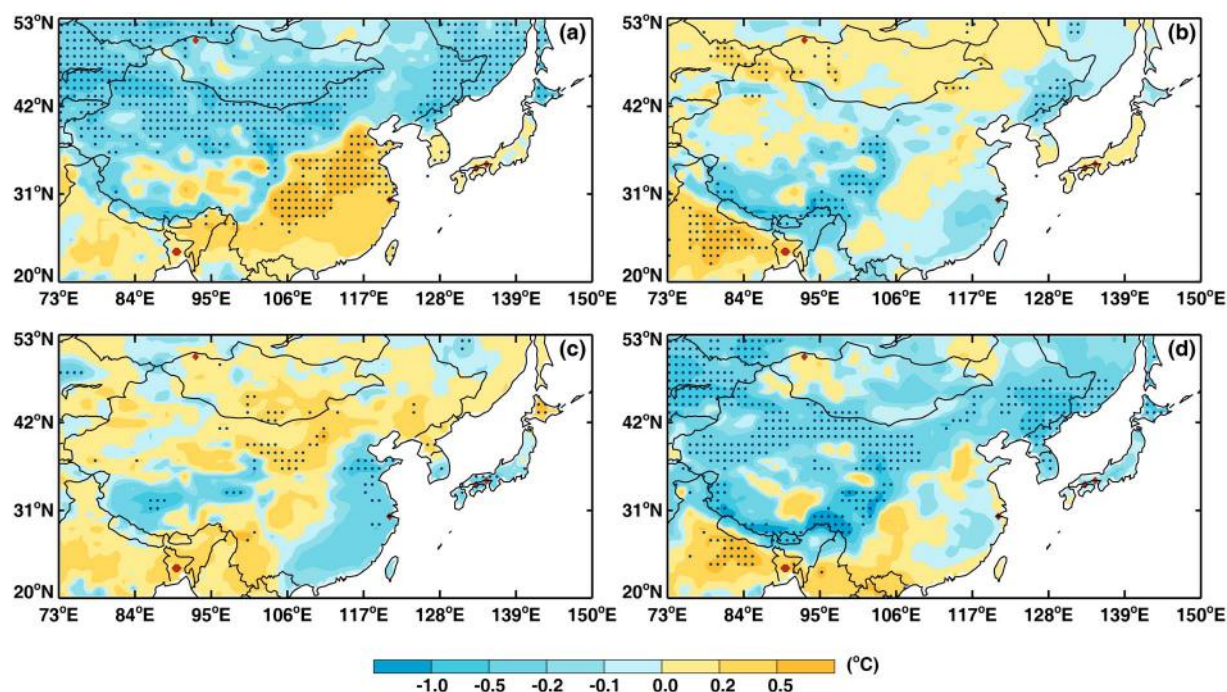**Figure 10.** Same as Figure 7 except for daily minimum temperature (°C).

Figure 11. Same as Figure 7 except for diurnal temperature range (°C).

Northwest China and a decrease in the humid region of Southeast China. Figure 11d shows that the three combined radiative factors induce a DTR decrease in most regions. It is consistent with the previous studies of DTR based on observational data, which showed that the DTR decreased on a global scale because of the strong increase in the daily minimum temperature [*Karl et al.*, 1984, 1993; *Kukla and Karl*, 1993]. The obvious decrease of DTR in China has been studied by *Chen and Chen* [2007], and other related analyses focused on the effects of clouds, solar radiation, soil moisture, surface wind, and precipitation on DTR [*Dai et al.*, 1999; *Zhou et al.*, 2009; *Wang et al.*, 2013].

To further explore the DTR response to CO_2, BC, and SO_4 changes over different types of climate regions, we calculated the changes of DTR as a function of the AI, shown in Figure 12. In nearly all the dry and humid regions, the DTR decreases in response to the three combined factors (green) and presents greater changes in drylands compared with those in humid regions. CO_2 (red) has the most significant influence on the DTR change. In arid regions, the DTR shows the greatest decrease, which reaches −0.31°C. In the humid regions with large AI, the DTR increases in response to CO_2, and in the regions with AI between 1.6 and 1.8, the increased amplitude is the highest. BC and SO_4 do not present obvious impacts on DTR. The influence of CO_2 on temperature is mainly via the absorption and emission of longwave radiation; hence, it leads to the warming of both daily maximum and minimum temperatures and induces the change of DTR.

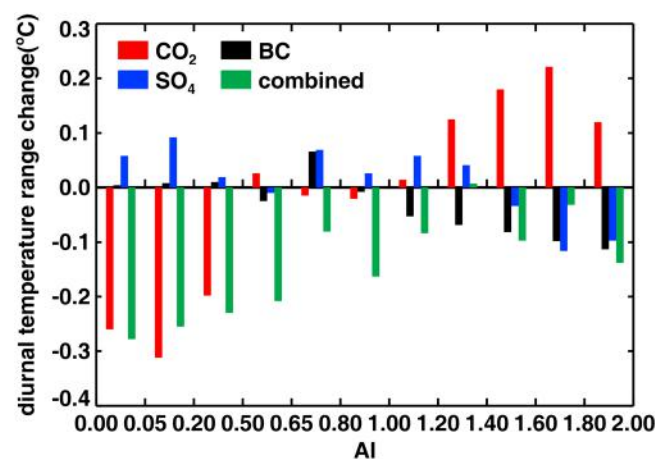**Figure 12.** Same as Figure 8 except for diurnal temperature range (°C).

5. Summary and Discussion

In this paper, we focus on the contributions of CO_2, BC, and SO_4 to enhanced dryland warming. Our results demonstrate that the enhanced warming in

the drylands of East Asia was mainly induced by CO_2 and BC, because temperature responses showed the greatest sensitivity to both CO_2 and BC in the drylands. The influence of CO_2 on temperature is most obvious over Northwest China. The influence of BC on temperature is most obvious over Tibet and Northeast China, because the BC in snow/ice regions shows an enhanced impact on temperature increase [*Ye et al.*, 2012; *Xu et al.*, 2016]. Compared with CO_2 and BC, SO_4 has a negative impact on temperature, and its influence on temperature is most obvious in Northeast China because of the high concentration of SO_4 in the region. The effects of the radiative factors are not limited to the mean temperature but extend to the daily maximum and minimum temperature as well. Daily maximum and minimum temperatures show asymmetric responses over different climate regions, inducing changes in DTR. In general, the DTR decreases in response to the three combined radiative factors. However, the DTR's response to CO_2 decreases in drylands and increases in humid regions.

Different from the mean temperature, DTR has important ecological significance [*Chen and Chen*, 2007]. Determining changes in DTR is considered a suitable method for investigating the counteracting effects of longwave and shortwave radiative forcing [*Makowski et al.*, 2008], and it has been promoted as a new indicator for climate change [*Stone and Weaver*, 2003; *Braganza et al.*, 2004; *Lewis and Karoly*, 2013]. Previous studies on the reduction of DTR in a warming climate noted large changes in cloud cover, sunshine duration [*Xia*, 2013], soil moisture, snow cover, and precipitation variability [*Cao et al.*, 1992; *Karl et al.*, 1993; *Stone and Weaver*, 2003; *Zhang et al.*, 2009; *Zhou et al.*, 2009; *Lauritsen and Rogers*, 2012; *Wang et al.*, 2014]. Generally, these forcing factors can be divided into natural forcing (volcanic aerosols and solar variability) and anthropogenic forcing (anthropogenic GHG and aerosols) [*Liu et al.*, 2016].

Observational analyses have attributed reductions in DTR primarily to increase in cloud cover and secondarily to increases in precipitation and soil moisture [e.g., *Dai et al.*, 1999]. However, large decrease in the DTR was observed over East China, where considerable decrease in cloud cover was found [*Kaiser*, 1998; *Liu et al.*, 2004; *Zhou et al.*, 2009]. Studies have suggested that the observed global trend in DTR is primarily caused by anthropogenic forcing [e.g., *Zhou et al.*, 2010; *Lewis and Karoly*, 2013]. Model simulations demonstrated that anthropogenic forcing plays a dominant role in the declining trend of DTR over Asia, where the GHG forcing is the main factor [*Liu et al.*, 2016]. Anthropogenic aerosol forcing also contributes to the decreasing trend in DTR over China, especially over East China [*Liu et al.*, 2016], which is consistent with the results of this study. However, we illustrate that DTR shows an opposite response to CO_2 over drylands and humid regions in this study. Further investigations are required to explore the mechanisms underlying the effects of CO_2, anthropogenic aerosols, and their interactions on DTR, especially in terms of differences in DTR over regions with different climate types.

References

Barnett, J., and S. O'Neill (2010), Maladaptation, *Global Environ. Change*, 20, 211–213, doi:10.1016/j.gloenvcha.2009.11.004.

Bi, J., J. Huang, Q. Fu, X. Wang, J. Shi, W. Zhang, Z. Huang, and B. Zhang (2011), Toward characterization of the aerosol optical properties over Loess Plateau of Northwestern China, *J. Quant. Spectrosc. Radiat. Transfer*, 112(2), 346–360, doi:10.1029/2009JD013372.

Bond, T. C., et al. (2013), Bounding the role of black carbon in the climate system: A scientific assessment, *J. Geophys. Res. Atmos.*, 118, 5380–5552, doi:10.1002/jgrd.50171.

Braganza, K., D. J. Karoly, and J. M. Arlaster (2004), Diurnal temperature range as an index of global climate change during the twentieth century, *Geophys. Res. Lett.*, 31, L13217, doi:10.1029/2004GL019998.

Cao, H. X., J. F. B. Mitchell, and J. R. Lavery (1992), Simulated diurnal range and variability of surface temperature in a global climate model for present and doubled CO_2 climates, *J. Clim.*, 5, 920–943.

Chen, B., J. Huang, P. Minnis, Y. Hu, Y. Yi, D. Zhang, and X. Wang (2010), Detection of dust aerosol by combining CALIPSO active lidar and passive IIR measurements, *Atmos. Chem. Phys.*, 10(9), 4241–4251, doi:10.5194/acp-10-4241-2010.

Chen, T. X., and X. Chen (2007), Variation of diurnal temperature range in China in the past 50 years, *Plateau Meteorol.*, 26(1), 150–157 (in Chinese).

Cook, K. H., and E. K. Vizy (2015), Detection and analysis of an amplified warming of the Sahara Desert, *J. Clim.*, 28(16), 6560–6580, doi:10.1175/JCLI-D-14-00230.1.

Dai, A., K. E. Trenberth, and T. R. Karl (1999), Effects of clouds, soil, moisture, precipitation, and water vapor on diurnal temperature range, *J. Clim.*, 12, 2451–2473, doi:10.1175/1520-0442(1999)012%3C2451:EOCSMP%3E2.0.CO;2.

Evan, A. T., J. P. Kossin, C. E. Chung, and V. Ramanathan (2011), Arabian Sea tropical cyclones intensified by emissions of black carbon and other aerosols, *Nature*, 479, 94–97, doi:10.1038/nature10552.

Feng, S., and Q. Fu (2013), Expansion of global drylands under a warming climate, *Atmos. Chem. Phys.*, 13(19), 10,081–10,094, doi:10.5194/acp-13-10081-2013.

Gao, Y., C. Zhao, X. Liu, M. Zhang, and L. R. Leung (2014), WRF-Chem simulations of aerosols and anthropogenic aerosol radiative forcing in East Asia, *Atmos. Environ.*, 92, 250–266, doi:10.1016/j.atmosenv.2014.04.038.

Guan, X., J. Huang, N. Guo, J. Bi, and G. Wang (2009), Variability of soil moisture and its relationship with surface albedo and soil thermal parameters over the Loess Plateau, *Adv. Atmos. Sci.*, 26(4), 692–700, doi:10.1007/s00376-009-8198-0.1.

Guan, X., J. Huang, R. Guo, H. Yu, P. Lin, and Y. Zhang (2015), Role of radiatively forced temperature changes in enhanced semi-arid warming in the cold season over east Asia, *Atmos. Chem. Phys.*, *15*(23), 13,777–13,786, doi:10.5194/acp-15-13777-2015.

Guan, X., J. Huang, Y. Zhang, Y. Xie, and J. Liu (2016), The relationship between anthropogenic dust and population over global semi-arid regions, *Atmos. Chem. Phys.*, *16*(8), 5159–5169, doi:10.5194/acp-16-5159-2016.

Hansen, J., R. Ruedy, M. Sato, and K. Lo (2010), Global surface temperature change, *Rev. Geophys.*, *48*, RG4004, doi: 10.1029/2010RG000345.

He, Y., J. Huang, and M. Ji (2014), Impact of land–sea thermal contrast on interdecadal variation in circulation and blocking, *Clim. Dyn.*, *43*(12), 3267–3279, doi:10.1007/s00382-014-2103-y.

Hsu, N. C., R. Gautam, A. M. Sayer, C. Bettenhausen, C. Li, M. J. Jeong, S.-C. Tsay, and B. N. Holben (2012), Global and regional trends of aerosol optical depth over land and ocean using SeaWiFS measurements from 1997 to 2010, *Atmos. Chem. Phys.*, *12*(17), 8037–8053, doi:10.5194/acp-12-8037-2012.

Hu, Y., and Y. Gao (1994), Some new understandings of processes at the land surface in arid area from the HEIFE [in Chinese], *Acta. Meteor. Sin.*, *52*(3), 285–296.

Huang, H., G. E. Thomas, and R. G. Grainger (2010), Relationship between wind speed and aerosol optical depth over remote ocean, *Atmos. Chem. Phys.*, *10*(13), 5943–5950, doi:10.5194/acp-10-5943-2010.

Huang, J., P. Minnis, B. Lin, Y. Yi, M. Khaiyer, R. Arduini, A. Fan, and G. Mace (2005), Advanced retrievals of multilayered cloud properties using multispectral measurements, *J. Geophys. Res.*, *110*, D15S18, doi:10.1029/2004JD005101.

Huang, J., B. Lin, P. Minnis, T. Wang, X. Wang, Y. Hu, Y. Yi, and J. K. Ayers (2006), Satellite-based assessment of possible dust aerosols semi-direct effect on cloud water path over East Asia, *Geophys. Res. Lett.*, *33*, L19802, doi:10.1029/2006GL026561.

Huang, J., et al. (2008), An overview of the semi-arid climate and environment research observatory over the Loess Plateau, *Adv. Atmos. Sci.*, *25*(6), 906–921, doi:10.1007/s00376-008-0906-7.

Huang, J., Q. Fu, W. Zhang, X. Wang, R. Zhang, H. Ye, and S. Warren (2011), Dust and black carbon in seasonal snow across northern China, *Bull. Am. Meteorol. Soc.*, *92*, 175–181, doi:10.1175/2010BAMS3064.1.

Huang, J., X. Guan, and F. Ji (2012), Enhanced cold-season warming in semi-arid regions, *Atmos. Chem. Phys.*, *12*(12), 5391–5398, doi:10.5194/acp-12-5391-2012.

Huang, J., M. Ji, Y. Liu, L. Zhang, and D. Gong (2013), Review of climate change research in arid and semi-arid regions [in Chinese], *Adv. Clim. Change Res.*, *9*, 9–14.

Huang, J., T. Wang, W. Wang, Z. Li, and H. Yan (2014), Climate effects of dust aerosols over East Asian arid and semi-arid regions, *J. Geophys. Res. Atmos.*, *119*, 11,398–11,416, doi:10.1002/2014JD021796.

Huang, J. P., J. J. Liu, B. Chen, and S. L. Nasiri (2015a), Detection of anthropogenic dust using CALIPSO lidar measurements, *Atmos. Chem. Phys.*, *15*(20), 11,653–11,665, doi:10.5194/acp-15-11653-2015.

Huang, J., M. Ji, Y. Xie, S. Wang, Y. He, and J. Ran (2015b), Global semi-arid climate change over last 60 years, *Clim. Dyn.*, *46*(3), 1131–1150, doi:10.1007/s00382-015-2636-8.

Huang, J., H. Yu, X. Guan, G. Wang, and R. Guo (2016), Accelerated dryland expansion under climate change, *Nat. Clim. Change*, *6*, 166–171, doi:10.1038/nclimate2837.

Ji, F., Z. Wu, J. Huang, and E. P. Chassignet (2014), Evolution of land surface air temperature trend, *Nat. Clim. Change*, *4*, 462–466, doi:10.1038/NCLIMATE2223.

Jin, Q., J. Wei, Z.-L. Yang, B. Pu, and J. Huang (2015), Consistent response of Indian summer monsoon to Middle East dust in observations and simulations, *Atmos. Chem. Phys.*, *15*(11), 9897–9915, doi:10.5194/acp-15-9897-2015.

Kaiser, D. P. (1998), Analysis of total cloud amount over China, 1951–1994, *Geophys. Res. Lett.*, *25*, 3599–3602, doi:10.1029/98GL52784.

Karl, T. R., B. Kukla, and J. Gavin (1984), Decreasing diurnal temperature range in the United States and Canada from 1941 through 1980, *J. Clim. Appl. Meteorol.*, *23*(11), 1489–1504, doi:10.1175/1520-0450(1984)023<1489:DDTRIT>2.0.CO;2.

Karl, T. R., P. D. Jones, R. W. Knight, G. Kukla, N. Plummer, V. Razuvayev, K. P. Gallo, J. Lindsay, R. J. Charlson, and T. C. Peterson (1993), Asymmetric trends of daily maximum and minimum temperature, *Bull. Am. Meteorol. Soc.*, *74*, 1007–1023.

Kasoar, M., A. Voulgarakis, J. F. Lamarque, D. T. Shindell, N. Bellouin, G. Faluvegi, and K. Tsigaridis (2016), Regional and global temperature response to anthropogenic SO$_2$ emissions from China in three climate models, *Atmos. Chem. Phys.*, *16*(15), 9785–9804, doi:10.5194/acp-16-9785-2016.

Kukla, G., and T. R. Karl (1993), Nighttime warming and the greenhouse effect, *Environ. Sci. Technol.*, *27*(8), 1468–1474, doi:10.1021/es00045a001.

Lamarque, J. F., et al. (2010), Historical (1850–2000) gridded anthropogenic and biomass burning emissions of reactive gases and aerosols: Methodology and application, *Atmos. Chem. Phys.*, *10*(15), 7017–7010, doi:10.5194/acp-10-7017-2010.

Lau, W. K. M., M. K. Kim, K. M. Kim, and W. S. Lee (2010), Enhanced surface warming and accelerated snowmelt in the Himalayas and Tibetan Plateau induced by absorbing aerosols, *Environ. Res. Lett.*, *5*, 025204, doi:10.1088/1748-9326/5/2/025204.

Lauritsen, R. G., and J. C. Rogers (2012), U.S. diurnal temperature range variability and regional causal mechanisms, 1901–2002, *J. Clim.*, *25*(20), 7216–7231, doi:10.1175/JCLI-D-11-00429.1.

Lewis, S. C., and D. J. Karoly (2013), Evaluation of historical diurnal temperature range trends in CMIP5 models, *J. Clim.*, *26*(22), 9077–9089, doi:10.1175/JCLI-D-13-00032.1.

Li, Y., and X. Zhao (2012), An empirical study of the impact of human activity on long-term temperature change in China: A perspective from energy consumption, *J. Geophys. Res.*, *117*, D17117, doi:10.1029/2012JD018132.

Li, Z., F. Niu, J. Fan, Y. Liu, D. Rosenfeld, and Y. Ding (2011), Long-term impacts of aerosols on the vertical development of clouds and precipitation, *Nat. Geosci.*, *4*, 888–894, doi:10.1038/NGEO1313.

Lin, L., A. Gettelman, S. Feng, and Q. Fu (2015), Simulated climatology and evolution of aridity in the 21st century, *J. Geophys. Res. Atmos.*, *120*, 5795–5815, doi:10.1002/2014JD022912.

Lin, L., Z. Wang, Y. Xu, and Q. Fu (2016a), Sensitivity of precipitation extremes to radiative forcing of greenhouse gases and aerosols, *Geophys. Res. Lett.*, *43*, 9860–9868, doi:10.1002/2016GL070869.

Lin, L., A. Gettelman, Q. Fu, and Y. Xu (2016b), Simulated differences in 21st century aridity due to different scenarios of greenhouse gases and aerosols, *Clim. Change*, 1–16, doi:10.1007/s10584-016-1615-3.

Lin, L., A. Gettelman, Y. Xu, and Q. Fu (2016c), Simulated responses of terrestrial aridity to black carbon and sulfate aerosols, *J. Geophys. Res. Atmos.*, *121*, 785–794, doi:10.1002/2015JD024100.

Liu, B., M. Xu, M. Henderson, Y. Qi, and Y. Li (2004), Taking China's temperature: Daily range, warming trends, and regional variations, 1955–2000, *J. Clim.*, *17*(22), 4453–4462, doi:10.1175/3230.1.

Liu, L., Z. Li, X. Yang, H. Gong, C. Li, and A. Xiong (2016), The long-term trend in the diurnal temperature range over Asia and its natural and anthropogenic causes, *J. Geophys. Res. Atmos.*, *121*, 3519–3533, doi:10.1002/2015JD024549.

Liu, Y., J. Huang, G. Shi, T. Takamura, P. Khatri, J. Bi, J. Shi, T. Wang, X. Wang, and B. Zhang (2011), Aerosol optical properties and radiative effect determined from sky-radiometer over Loess Plateau of Northwest China, *Atmos. Chem. Phys.*, *11*(22), 11455–11463, doi:10.5194/acp-11-11455-2011.

Lu, X., L. Wang, and M. F. McCabe (2016), Elevated CO_2 as a driver of global dryland greening, *Sci. Rep.*, *6*, 20716, doi:10.1038/srep20716.

Mahowald, N. M., and C. Luo (2003), A less dusty future?, *Geophys. Res. Lett.*, *30*(17), 1903, doi:10.1029/2003GL017880.

Makowski, K., M. Wild, and A. Ohmura (2008), Diurnal temperature range over Europe between 1950 and 2005, *Atmos. Chem. Phys.*, *8*(2), 7051–7084, doi:10.5194/acpd-8-7051-2008.

Meehl, G. A., W. M. Washington, J. M. Arblaster, A. Hu, H. Teng, J. E. Kay, A. Gettelman, D. M. Lawrence, B. M. Sanderson, and W. G. Strand (2013), Climate change projections in CESM1(CAM5) compared to CCSM4, *J. Clim.*, *26*(17), 6287–6308, doi:10.1175/JCLI-D-12-00572.1.

Middleton, N., and D. Thomas (Eds.) (1997), *World Atlas of Desertification*, 2nd ed., 182 pp., UNEP, Edward Arnold, Hodder Headline, London.

Mitchell, T. D., and P. D. Jones (2005), An improved method of constructing a database of monthly climate observations and associated high-resolution grids, *Int. J. Climatol.*, *25*(6), 693–712, doi:10.1002/joc.1181.

Morrison, H., and A. Gettelman (2008), A new two-moment bulk stratiform cloud microphysics scheme in the community atmosphere model, version 3 (CAM3). Part I: Description and numerical tests, *J. Clim.*, *21*, 3642–3659, doi:10.1175/2008JCLI2105.1.

Myhre, G., et al. (2013), Anthropogenic and natural radiative forcing, in *Climate Change 2013: The Physical Science Basis. Contribution of Working Group I to the Fifth Assessment Report of the Intergovernmental Panel on Climate Change*, edited by T. F. Stocker et al., pp. 659–740, Cambridge Univ. Press, Cambridge, U. K., and New York.

Qian, Y., and C. Fu (1997), Sulfur dioxide emission, sulfate aerosol and climate change [in Chinese], *Adv. Earth Sci.*, *12*(5), 440–446.

Qian, Y., W. I. Gustafson, L. R. Leung, and S. J. Ghan (2009), Effects of soot-induced snow albedo change on snowpack and hydrological cycle in western United States based on Weather Research and Forecasting chemistry and regional climate simulations, *J. Geophys. Res.*, *114*, D03108, doi:10.1029/2008JD011039.

Qian, Y., M. G. Flanner, L. R. Leung, and W. Wang (2011), Sensitivity studies on the impacts of Tibetan Plateau snowpack pollution on the Asian hydrological cycle and monsoon climate, *Atmos. Chem. Phys.*, *11*(5), 1929–1948, doi:10.5194/acp-11-1929-2011.

Santer, B. D., et al. (2005), Amplification of surface temperature trends and variability in the tropical atmosphere, *Science*, *309*(5740), 1551–1556, doi:10.1126/science.1114867.

Smoliak, B. V., J. M. Wallace, P. Lin, and Q. Fu (2015), Dynamical adjustment of the Northern Hemisphere surface air temperature field: Methodology and application to observations, *J. Clim.*, *28*(4), 1613–1629, doi:10.1175/JCLI-D-14-00111.1.

Stocker T. F., et al. (Eds.) (2013), *Climate Change 2013: The Physical Science Basis, Contribution of Working Group I to the Fifth Assessment Report of the Intergovernmental Panel on Climate Change*, pp. 3–29, Cambridge Univ. Press, Cambridge, U. K., and New York, doi:10.1017/CBO9781107415324.020.

Stone, A., and J. Weaver (2003), Factors contributing to diurnal temperature range trends in twentieth and twenty-first century simulations of the CCCma coupled model, *Clim. Dyn.*, *20*(5), 435–445, doi:10.1007/s00382-002-0288-y.

Thorne, P. W., J. R. Lanzante, T. C. Peterson, D. J. Seidel, and K. P. Shine (2010), Tropospheric temperature trends: History of an ongoing controversy, *Wiley Interdiscip. Rev. Clim. Change*, *2*, 66–88, doi:10.1002/wcc.80.

Twomey, S. (1977), The influence of pollution on the shortwave albedo of clouds, *J. Atmos. Sci.*, *34*(7), 1149–1152, doi:10.1175/1520-0469(1977)034<1149:TIOPOT>2.0.CO;2.

Ukkola, A. M., I. C. Prentice, T. F. Keenan, A. I. J. M. van Dijk, N. R. Viney, R. B. Myneni, and J. Bi (2015), Reduced streamflow in water-stressed climates consistent with CO2 effects on vegetation, *Nat. Clim. Change*, *6*(2009), 75–78, doi:10.1038/nclimate2831.

Wallace, J. M., Q. Fu, B. V. Smoliak, P. Lin, and C. M. Johanson (2012), Simulated versus observed patterns of warming over the extratropical Northern Hemisphere continents during the cold season, *Proc. Natl. Acad. Sci. U.S.A.*, *109*(36), 14,337–14,342, doi:10.1073/pnas.1204875109.

Wang, F., C. Zhang, Y. Peng, and H. Zhou (2014), Diurnal temperature range variation and its causes in a semiarid region from 1957 to 2006, *Int. J. Climatol.*, *34*(2), 343–354, doi:10.1002/joc.3690.

Wang, K., and R. E. Dickinson (2013), Contribution of solar radiation to decadal temperature variability over land, *Proc. Natl. Acad. Sci. U.S.A.*, *110*(37), 14,877–14,882, doi:10.1073/pnas.1311433110.

Wang, K., R. E. Dickinson, and S. Liang (2012), Global atmospheric evaporative demand over land from 1973 to 2008, *J. Clim.*, *25*(23), 8353–8361, doi:10.1175/JCLI-D-11-00492.1.

Wang, X., S. J. Doherty, and J. Huang (2013), Black carbon and other light-absorbing impurities in snow across Northern China, *J. Geophys. Res. Atmos.*, *118*, 1471–1492, doi:10.1029/2012JD018291.

White, R. P., and J. Nackoney (2003), Drylands, people, and ecosystem goods and services: A web-based geospatial analysis, World Resources Institute. [Available at http://s1.downloadmienphi.net/file/downloadfile6/151/1384326.pdf.]

Xia, X. (2013), Variability and trend of diurnal temperature range in China and their relationship to total cloud cover and sunshine duration, *Ann. Geophys.*, *31*(5), 795–804, doi:10.5194/angeo-31-795-2013.

Xu, X., and J. Wang (2015), Retrieval of aerosol microphysical properties from AERONET photopolarimetric measurements: 1. Information content analysis, *J. Geophys. Res. Atmos.*, *120*, 7059–7078, doi:10.1002/2015JD023108.

Xu, X., et al. (2015), Retrieval of aerosol microphysical properties from AERONET photopolarimetric measurements: 2. A new research algorithm and case demonstration, *J. Geophys. Res. Atmos.*, *120*, 7079–7098, doi:10.1002/2015JD023113.

Xu, Y. (2014), *Climate Effects of Black Carbon and the Emission Reduction for Mitigating Climate Change*, pp. 1–22, Univ. of California, San Diego, Calif.

Xu, Y., and S. P. Xie (2015), Ocean mediation of tropospheric response to reflecting and absorbing aerosols, *Atmos. Chem. Phys.*, *15*(10), 5827–5833, doi:10.5194/acp-15-5827-2015.

Xu, Y., R. Bahadur, C. Zhao, and L. Ruby Leung (2013), Estimating the radiative forcing of carbonaceous aerosols over California based on satellite and ground observations, *J. Geophys. Res. Atmos.*, *118*, 11,148–11,160, doi:10.1002/jgrd.50835.

Xu, Y., V. Ramanathan, and W. M. Washington (2016), Observed high-altitude warming and snow cover retreat over Tibet and the Himalayas enhanced by black carbon aerosols, *Atmos. Chem. Phys.*, *16*(3), 1303–1315, doi:10.5194/acp-16-1303-2016.

Ye, H., R. Zhang, J. Shi, J. Huang, S. G. Warren, and Q. Fu (2012), Black carbon in seasonal snow across northern Xinjiang in northwestern China, *Environ. Res. Lett.*, *7*(4), 044002, doi:10.1088/1748-9326/7/4/044002.

Zhang, J., W.-C. Wang, and L. Wu (2009), Land-atmosphere coupling and diurnal temperature range over the contiguous United States, *Geophys. Res. Lett.*, *36*, L06706, doi:10.1029/2009GL037505.

Zhang, Q., G. Wei, and R. Huang (2001), Observation and study of atmospheric drag coefficients in Dunhuang [in Chinese], *Sci. China, Ser. D Earth Sci.*, *31*, 783–792.

Zhao, C., et al. (2014), Simulating black carbon and dust and their radiative forcing in seasonal snow: A case study over North China with field campaign measurements, *Atmos. Chem. Phys.*, *14*(20), 11,475–11,491, doi:10.5194/acp-14-11475-2014.

Zhou, L. (2016), Desert amplification in a warming climate, *Sci. Rep.*, *6*, 31065, doi:10.1038/srep31065.

Zhou, L., A. Dai, Y. Dai, R. S. Vose, C. Z. Zou, Y. Tian, and H. Chen (2009), Spatial dependence of diurnal temperature range trends on precipitation from 1950 to 2004, *Clim. Dyn.*, *32*(2–3), 429–440, doi:10.1007/s00382-008-0387-5.

Zhou, L., R. E. Dickinson, A. Dai, and P. Dirmeyer (2010), Detection and attribution of anthropogenic forcing to diurnal temperature range changes from 1950 to 1999: Comparing multi-model simulations with observations, *Clim. Dyn.*, *35*(7), 1289–1307, doi:10.1007/s00382-009-0644-2.

Zhou, L., H. Chen, W. Hua, Y. Dai, and N. Wei (2016), Mechanisms for stronger warming over drier ecoregions observed since 1979, *Clim. Dyn.*, *47*(9–10), 2955–2974, doi:10.1007/s00382-016-3007-9.